This document is the Accepted Manuscript version of a Published Work that appeared in final form in **ACS Applied Materials & Interfaces**, **copyright 2022 American Chemical Society** after peer review and technical editing by the publisher. To access the final edited and published work see https://doi.org/10.1021/acsami.2c18951.
Postprint of: Kamecki B., Cempura G., Jasiński P., Wang S., Molin S., Tuning Electrochemical Performance by Microstructural Optimization of the Nanocrystalline Functional Oxygen Electrode Layer for Solid Oxide Cells, ACS Applied Materials & Interfaces, Vol. 14,iss. 51 (2022), pp. 57449-57459

Tuning electrochemical performance by microstructural optimisation of nanocrystalline functional oxygen electrode layer for Solid Oxide Cells

Bartosz Kamecki[1,2*], Grzegorz Cempura[3], Piotr Jasiński[2], Sea-Fue Wang[4], Sebastian Molin[2]

[1] Advanced Materials Center, Faculty of Applied Physics and Mathematics, Gdańsk University of Technology, Gabriela Narutowicza street 11/12, 80-233 Gdańsk, Poland

[2] Advanced Materials Center, Faculty of Electronics, Telecommunications, and Informatics, Gdańsk University of Technology, Gabriela Narutowicza street 11/12, 80-233 Gdańsk, Poland

[3] International Centre for Electron Microscopy, Faculty of Metals Engineering and Industrial Computer Science, AGH University of Science and Technology, Adama Mickiewicza street 30, 30-059 Kraków, Poland

[4] Department of Materials and Mineral Resources Engineering, National Taipei University of Technology, No.1, Sec. 3, Zhongxiao E. Rd., Taipei, 106, Taiwan

*corresponding author: bartosz.kamecki@pg.edu.pl

Abstract:

Further development of solid oxide fuel cell (SOFC) oxygen electrodes can be achieved through improvements in oxygen electrode design by microstructure miniaturisation alongside nanomaterials implementation. In this work, improved electrochemical performance of an $La_{0.6}Sr_{0.4}Co_{0.2}Fe_{0.8}O_{3-d}$ (LSCF) cathode was achieved by the controlled modification of the $La_{0.6}Sr_{0.4}CoO_{3-d}$ (LSC) nanocrystalline interlayer introduced between a porous oxygen electrode and dense electrolyte. The evaluation was carried out for various LSC layer thicknesses, annealing temperatures, oxygen partial pressures, and temperatures, as well as subjected to long-term stability tests and evaluated in typical operating conditions in an intermediate temperature SOFC. Electrochemical impedance spectroscopy (EIS) and a distribution of relaxation times analysis (DRT) were performed to reveal the rate-limiting electrochemical processes that limit the overall electrode performance. The main processes with an impact on the electrode performance were the adsorption of gaseous oxygen O_2, dissociation of O_2, and charge transfer-diffusion (O^{2-}). The introduction of a nanoporous and nanocrystalline interlayer with extended electrochemically active surface area accelerates the oxygen surface exchange kinetics and oxygen ion diffusions, reducing polarisation resistances. The polarisation resistance of the reference LSCF was lowered by one order of magnitude from 0.77Ω·cm^2 to 0.076 Ω·cm^2 at 600°C by the deposition of a 400 nm LSC interlayer at the interface. The developed electrode tested in the anode-supported fuel cell configuration showed a higher cell performance by 20% compared to the

cell with the reference electrode. The maximum power density at 700°C reaches 675 and 820 mW·cm^{-2} for the reference cell and the cell with the LSC interlayer, respectively. Ageing tests at 700°C under a high load of 1 A·cm^2 were performed.

Keywords:

oxygen electrode interlayer, electrode-electrolyte interface, solid oxide fuel cells, spray pyrolysis, nanocrystalline layer, distribution of relaxation times, electrochemical impedance spectroscopy

1. Introduction

Hydrogen energy is a promising renewable resource for the sustainable development of society and has significant potential to accelerate the scale-up of clean and renewable energy[1,2]. Solid oxide cells (SOCs) are one of the technologies considered as clean and highly efficient in comparison to the current energy conversion and storage systems and can easily cooperate with renewable energy sources to produce hydrogen-based liquid fuels[3]. Besides the benefits from the use of SOCs, there are some technical issues to be solved. SOC systems require high operating temperatures of 800–1000°C which accelerates degradation processes, contributes to poor thermomechanical stability, and makes the use of nanomaterials impossible in that high-temperature range [4,5]. One of the main problems alongside reducing the operating temperatures is increasing the internal resistances of the electrolytes and electrodes. While it is possible to reduce the thickness of the electrolyte to reduce the ohmic resistance, the electrode materials require more sophisticated modifications to improve their performance at lower temperatures [6–8]. Progress in developing and understanding fuel and oxygen electrode materials at lower temperatures is needed. Special attention has been placed on oxygen electrodes, which often limit the overall performance of cells [9]. However, some groups report the overall performance of SOFC may be limited by both the cathode as well as anode[10,11].

Throughout the years, primarily electron-conducting electrodes such as $La_{1-x}Sr_xMnO_{3-d}$ (LSM) have been replaced by mixed ionic-electronic conductors such as $La_{0.6}Sr_{0.4}Co_{0.2}Fe_{0.8}O_{3-d}$ (LSCF) or $La_{0.6}Sr_{0.4}CoO_3$ (LSC). LSC is a very catalytically active material and is reported as a good material for infiltration and modification of the mixed conducting LSCF. Further improvement of the electrode microstructure has been achieved by the fabrication of nanocomposite cathodes, graded cathodes, infiltrated cathodes, and cathodes with an active functional layer [12–14]. All these modifications are linked with the application of nanoparticles or nanometric grains which lead to a well-developed microstructure and yield a higher TPB density, lower polarisation resistance, and improved redox stability [15]. However, LSC has reported a very high thermal expansion coefficient for dense bulk samples (i.e.~23 x 10^{-6} K^{-1})[16]. The TEC of commonly used electrolyte materials for SOFC applications, such as yttria-stabilized zirconia (i.e.~10.5 x 10^{-6} K^{-1}) or gadolinium doped ceria (i.e.~12.5 x 10^{-6} K^{-1})

MOST WIEDZY Downloaded from mostwiedzy.pl

differ substantially from the LSCF electrode (i.e.~14.8 x 10^{-6} K^{-1})[17] as well as LSC electrode. A large difference in reported thermal expansion coefficients may have an adverse effect on both thermal stress and lattice strain between the cathode and the electrolyte and can lead to delamination of the interface during thermal cycling. On the other hand, the reported TEC value of LSC mainly refers to dense bulk materials, not porous thin films. The value of the thermal expansion coefficient shows thickness dependence and is laterally constrained and expands along the thickness direction only due to the solid substrate[18].

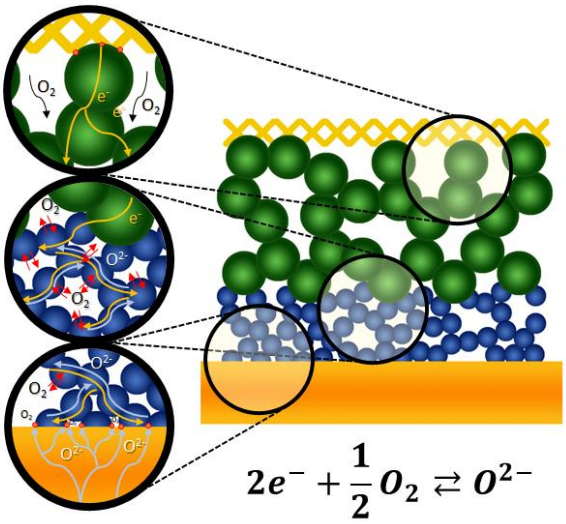

Figure 1. Schematic model of proposed modification with highlighted characteristic reaction occurring in the electrode.

This work evaluates the effects of the addition of a highly active interface interlayer of LSC between a porous LSCF electrode and $Ce_{0.8}Gd_{0.2}O_{1.9}$ electrolyte. Figure 1 shows a schematic representation of the model electrode interfaces with the occurring electrochemical reactions. LSCF is a mixed ionic electronic conducting material so the electrochemical reaction not only takes place at the electrode-electrolyte-gas interface but can also take place on the surface of the grains of the electrode material. The introduction of a thin <1 µm nanocrystalline MIEC layer between the macroporous electrode and electrolyte extends the electrochemically active surface area and reduces the individual resistances of rate-limiting reactions. Thus, performance improvement seems to be possible through the application of the nanoporous and nanocrystalline LSC electrode material at the electrode-electrolyte interface, but a detailed analysis of the impact of a modification on the final properties of the electrode is necessary.

MOST WIEDZY Downloaded from mostwiedzy.pl

2. Materials and Methods

For the electrochemical investigations, symmetrical samples of the developed electrode were prepared on dense $Ce_{0.8}Gd_{0.2}O_{2-d}$ (GDC-20K, Daiichi Kigenso Kagaku Kogyo Japan) pellets sintered at 1450°C for 5h and polished on both sides. An interlayer of electrochemically active LSC was prepared to utilise the spray pyrolysis technique on both sides of the pellets. Detailed characterisation of the crystal structure and microstructural properties of this layer was previously investigated and described elsewhere [19,20]. To investigate the influence of the interlayer thickness on the electrochemical performance, different amounts of LSC precursor (0.5, 1, 2, 4, and 8 ml) were sprayed onto pellets to obtain interlayer thicknesses of 50, 100, 200, 400, and 800 nm. The liquid precursors were prepared from 10 vol% of aqueous nitrate solutions of selected nitrates, $La(NO_3)_3 \cdot 6H_2O$ (Alfa Aesar, 99% purity), $Sr(NO_3)_2$ (Alfa Aesar, 99% purity), $Co(NO_3)_2 \cdot 6H_2O$ (Chempur, 98%), mixed with 90 vol% tetraethylene glycol (Sigma-Aldrich, 99% purity). The total concentration of cations in the precursor was fixed at 0.2 mol L^{-1}. The substrate temperature was 390°C and the polymer precursor flow rate was set to 2.5 ml/h. After the deposition process, approx. 30 µm of porous $La_{0.6}Sr_{0.4}Co_{0.2}Fe_{0.8}O_{3-d}$ (ESL Europe) was screen printed on top of the deposited layer and annealed at 600°C for 2h before the electrochemical measurements. Additional reference symmetrical samples without the interlayer at the interface were prepared and sintered at 600°C or 1050°C for 2h. For the fuel cell tests, anode-supported half-cells were used for oxygen electrode deposition. The half cells were produced by the National Taipei University of Technology (TaipeiTech, Taipei, Taiwan) by tape-casting/screen printing processes. The cells consist of a Ni-YSZ support, Ni-YSZ active electrode, and 8−10 µm thick YSZ electrolyte. More details about the cell microstructure and CGO barrier layer deposition can be found here [21,22]. Two types of cells were prepared: a reference cell and a cell with a 400 nm LSC layer on the interface between the electrolyte and the LSCF electrode

The microstructure of the samples was analysed by X-ray diffraction (XRD) using a Bruker D2 Phaser diffractometer with a Lynxeye XE-T detector with CuKα radiation (λ = 0.15406 nm) at room temperature. The morphology of the samples was investigated by scanning electron microscopy (FEI Quanta FEG 250) with an ET (Everhart–Thornley) secondary electron detector at an acceleration voltage of 20 kV. TEM investigations were performed in high resolution on a Titan Cubed G2 60-300 (FEI) Probe Cs corrected (S)TEM equipped with a ChemiSTEM EDX detector system based on four windowless Silicon Drift Detectors (Super X).

The electrochemical properties were measured using Solatron 1260 frequency analyser. Measurements were carried out in a frequency range of 100 kHz – 0.1 Hz with an excitation amplitude of 25 mV. The temperature was controlled by a PID controller contacted with a thermocouple placed

MOST WIEDZY Downloaded from mostwiedzy.pl

directly on the sample. The gas composition in the sealed quartz tube was controlled by mass flow controllers (Alicat Scientific). EIS data analysis was performed using the Elchemea Analytical software[23]. Distribution of Relaxation Times analysis was performed using the DRTools Matlab GUI [24]. The DRT analysis was performed by choosing the C4 Matern method of discretisation utilising the 2nd order of regularisation derivative and regularisation parameter (λ) of 10^{-4}.

Measurements of samples with different interlayer thicknesses were conducted in atmospheric air exposing the samples to different maximum annealing temperatures in four annealing-cooling cycles. The first measurement of the cycle was started after the isothermal holding of a sample at the evaluated annealing temperature i.e. 600°C for 2h and measured down to 400°C with 50°C steps. During the cooling down steps, the sample was held for one hour in isothermal conditions before the measurement. Each subsequent cycle was higher by 100°C until the last cycle of 900°C. The ASR_{pol} was obtained from the impedance spectra by the intercept of the spectra with the real axis divided by a factor of two and by multiplying the cathode polarisation resistance by the cathode area to account for the electrodes on both sides.

The dependence of the electrochemical response on different oxygen partial pressures was studied to support EIS spectra deconvolution by indicating the electrochemical reactions occurring in the electrode. $p(O_2)$ measurement starts with an isothermal holding of the sample overnight (16h) at 600°C in air and then the EIS spectra were measured at 0.1, 0.5, 1.5, 5, and 20 % oxygen concentration precisely controlled by mass flow controllers. The investigated temperatures were 600, 550, and 500°C. After the last measurement, the temperature was returned to 600°C and the sample was isothermally held in the air atmosphere for the next 100h.

Fuel cell characterisation was performed in an OpenFlanges V5 test setup (Fiaxell Sàrl Technologies). The prepared cell was electrically connected by a nickel mesh from the anode side and by an Au mesh from the cathode side. The cell was placed in a Kittec furnace with a process identifier temperature controller. The wires were connected to a Solartron 1260/1287 frequency analyser for impedance and current-voltage characterisation. The cell was heated to 700°C and isothermally held. The anode was reduced in dry H_2 used as a fuel supplied from the anode side and also synthetic air was delivered to the cathode as an oxidant. To characterise the cell, the impedance spectra were measured at OCV. For cell performance, current-voltage characteristics were measured. The ageing of the cell was performed in galvanostatic mode at current densities of 250, 500, and 1000 $mA \cdot cm^{-2}$.

MOST WIEDZY Downloaded from mostwiedzy.pl

3. Results and discussion

3.1 Description of the prepared layers used for testing

Figures 2 A, B, and C show XRD spectra of the bare CGO substrate and LSC layers on CGO substrates after different heat treatments. In the as-deposited state, the layer is amorphous and crystallises at approx. 600°C, as was previously studied for the layers on sapphire substrates [19]. The LSC peaks are marked according to PDF #00-36-1393, corresponding to the rhombohedral structure, though the cubic structure also fits well, in agreement with the literature [25]. The main LSC peaks (indexed as 110, 104) overlap with the main CGO peak (PDF #00-50-0201, (200) peak approx. 33.083°), therefore Figures 2 B and C present the magnified (012) and (202) peaks of the LSC, which show the formation of the perovskite phase.

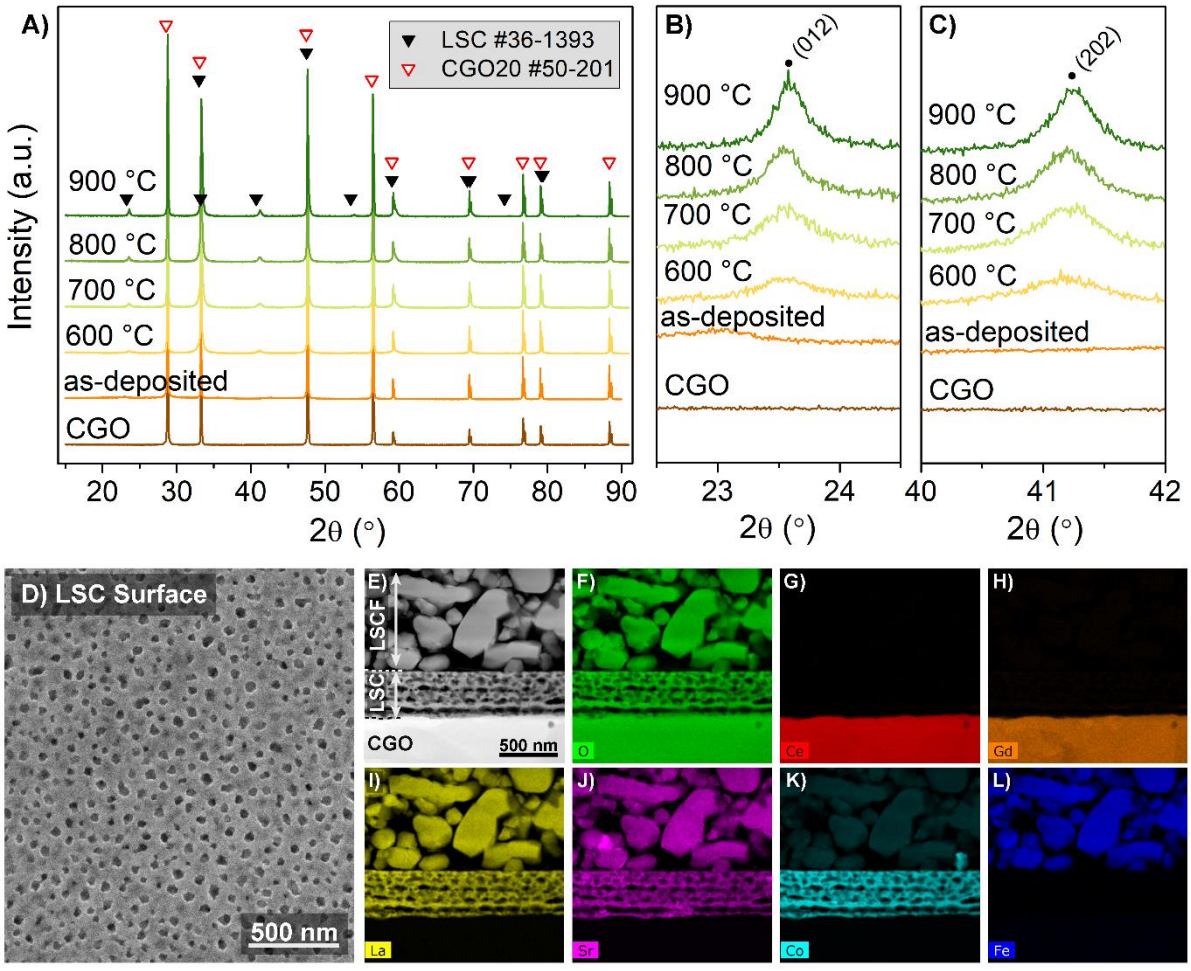

Figure 2. (A–C) X-ray diffractometry patterns of LSC layers deposited on CGO and annealed at different temperatures, D) SEM surface image of LSC layer annealed at 700°C for 2h, E) HAADF TEM cross-section image of electrode interface F–L) STEM-EDS distribution of elements maps.

MOST WIEDZY Downloaded from mostwiedzy.pl

Figures 2 D and E present the SEM (BSE) and TEM (HAADF) images of the LSC surface and cross-section after annealing at 700°C for 2h. No special features are visible on the surface, the whole surface is covered uniformly, with no cracks or delamination defects. Nanometric pores (d≈80 nm) are homogenously distributed over a whole surface area. The cross-section shows the LSC interface layer sandwiched between the CGO substrate and the current-collecting LSCF layer. The presented layer was prepared from a 4 ml liquid precursor, resulting in a thickness of approx. 400 nm. The LSC layer adheres very well to the CGO substrate and has smaller particles and small pores when compared to the LSCF current-collecting layer or traditionally powder-processed electrodes. The distribution of elements present in the sample were shown in Figures 2 F–L. There are no interactions between the electrolyte and electrode, while the distributions of the elements were homogenous and no segregation of the elements was observed.

3.2 Electrochemical tests of symmetrical cells

To evaluate the electrochemical performance towards the oxygen reduction/oxidation reaction, electrochemical impedance spectroscopy measurements were performed on symmetrical samples.

3.2.1 Influence of layer thickness

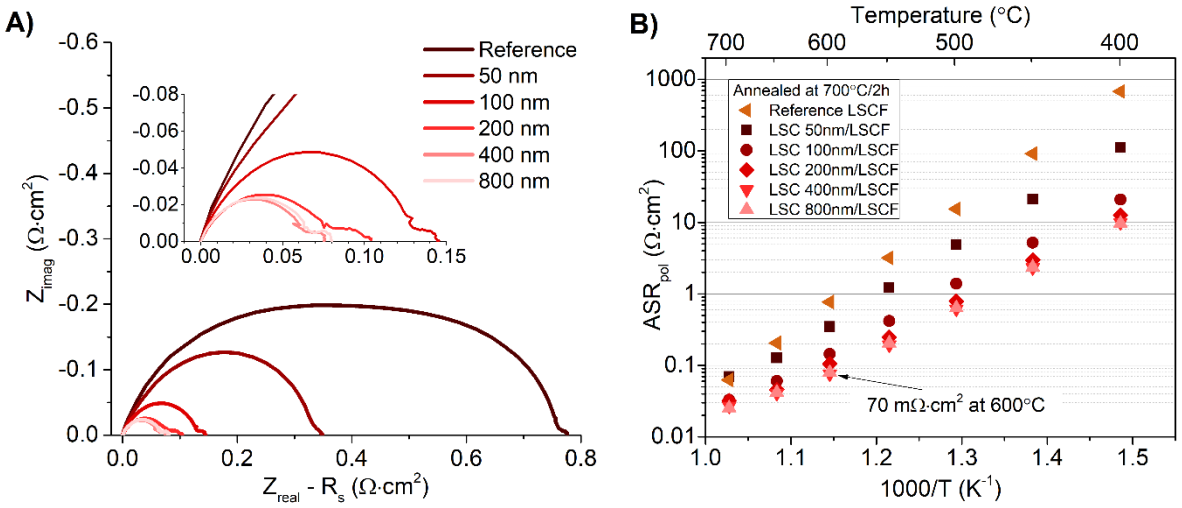

Figure 3. A) Nyquist plot and B) Polarisation resistances of the cells with different LSC interlayer thicknesses annealed at 700°C for 2h. Results for reference LSCF electrode annealed under the same conditions are included for comparison.

Figure 3 presents (A) Nyquist plot and (B) ASR_{pol} values as a function of temperature for reference and electrodes with the LSC interface layer annealed at 700°C for 2h. For clarity, the ohmic resistance has been subtracted. The ASR_{pol} values of the samples with the interfacial layer are much lower in comparison with the reference sample. The addition of even the thinnest layer (approx. 50 nm) of LSC

MOST WIEDZY Downloaded from mostwiedzy.pl

at the interface reduces the polarisation resistance, which is further improved by increasing the thickness of the interfacial layer. The ASR_{pol} values measured at 600°C were 0.349; 0.145; 0.105; 0.079 and 0.076 Ω·cm^2 for samples with 50, 100, 200, 400 and 800 nm of LSC interlayer thickness, while ASR_{pol} for the reference LSCF without interface modification was 0.77Ω·cm^2. The decreasing ASR_{pol} with the increasing LSC thickness could be correlated with the thickness of the electrochemically active layer of a nanoporous electrode with mixed ion-electron conductivity. In the beginning, increasing the thickness of the LSC electrode decreases the polarisation resistance due to a larger surface area becoming available for the reaction at the LSC interlayer/gas interface. As explained by Liu, the thickness of the electrochemically active layer of a porous MIEC electrode decreases with the increased rate of surface reaction and with decreased transport of ionic or electronic defects in the LSC interlayer [26]. Thus, the deposition of the nanoporous LSC interlayer with a higher surface exchange property than LSCF [27] makes it possible to reduce the thickness of the whole electrode. At some interlayer thickness, the ASR_{pol} results do not further decrease. The results obtained for the 400 nm and 800 nm are similar, which is most likely related to the limitations of charge transfer through the electrolyte layer. This may hint that LSCF serves as the current collector not the electrochemical catalyst for the oxygen reduction reaction. Therefore, for certain thicknesses of the LSC interlayer, LSC becomes the effective cathode layer, and LSCF acts then merely as a current collector. Thus, for the remaining studies, 400 nm thick LSC was selected as the sample for more extensive evaluations.

3.2.2 Influence of annealing temperature.

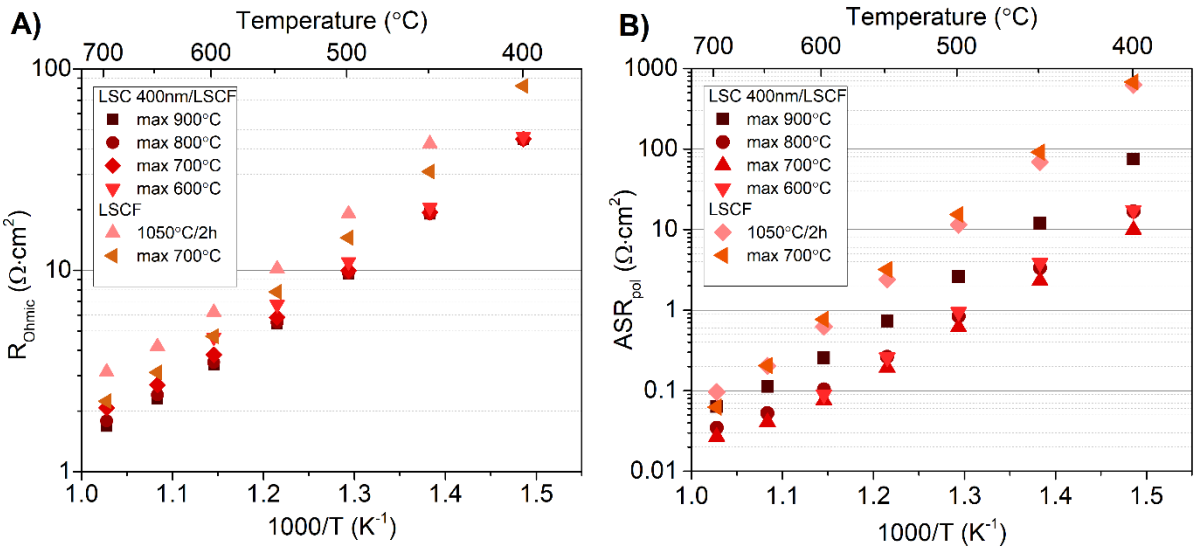

Figure 4. A) Ohmic and B) polarisation resistances of the cells with 400 nm thick LSC interlayer annealed at different temperatures. Results for reference LSCF are included for comparison.

MOST WIEDZY Downloaded from mostwiedzy.pl

The next step was an evaluation of the influence of the annealing temperature and microstructural features on the electrode performance. As was described in our previous work [19], the post-processing temperature has a strong influence on the layer microstructure by determining their porosity and grain dimensions. The main goal was to find the best microstructure for the highest electrochemical efficiency of the electrode. The R_{ohmic} and ASR_{pol} values for different annealing temperatures of a sample with a 400 nm LSC interlayer are presented in Figure 4. As can be seen, increasing the annealing temperature reduces the ohmic resistance of the electrode-electrolyte interface, reaching a minimum for the sample annealed at 900°C. This may explain the better adhesion of the layer to the electrolyte. However, the polarisation resistance also reaches the minimum for the sample annealed at 700°C, indicating the best microstructural features for the best electrochemical performance. A further increase in the annealing temperature results in a significantly increasing polarisation resistance. This phenomenon is related to the high surface area available for the oxygen surface exchange reaction in layers annealed at lower temperatures, resulting from the nanoscaled microstructure and enhanced oxygen surface exchange properties of LSC. Figure S1 in supplementary materials presents SEM images of polished cross-sections of samples annealed at a temperature range of 600 - 900°C for 2h. As can be noticed, the LSC layer microstructure significantly changes by increasing grain dimensions due to coarsening of nanoparticles after annealing above 700°C. However, at the intermediate temperature range of 600 – 700°C interlayer microstructure remains nanocrystalline and is the same for both temperatures. Increasing the annealing temperature leads to increased growth and reduced porosity of the layer, which reduces the number of available catalytically active sites and leads to an increase in the polarisation resistance. A similar observation was noticed by Hayd et al. [28] in nanoscaled LSC electrodes produced by the metal-organic deposition (MOD) method, where the highest electrode activity was reported for electrodes processed at 700°C. In the other work, Develos-Bagarinao et al. investigated the influence of the deposition temperature and long-term annealing on LSC thin films deposited by Pulsed Layer Deposition (PLD)[29]. In their research, a significant improvement in the electrode performance was also achieved by enhancing the surface exchange property as mediated by a distinctive nanostructure that retains the high porosity, and the better stability of the electrode-electrolyte interfaces [29].

3.2.3 Impedance Data Analysis

To better understand the mechanisms occurring in the developed electrode, a detailed analysis of the collected EIS data was performed. A representative sample with 400 nm of LSC interlayer was measured at different oxygen partial pressures.

MOST WIEDZY Downloaded from mostwiedzy.pl

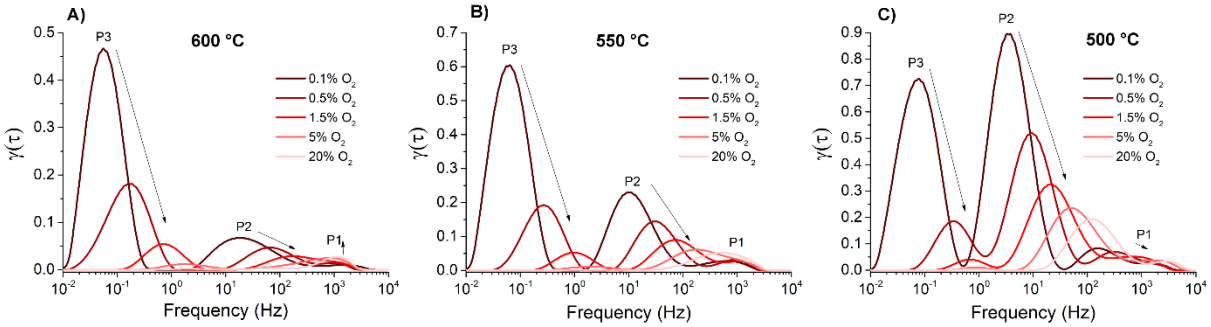

Figure 5. DRT analysis results for a sample with a 400 nm LSC interlayer at the interface. Results compare deconvoluted EIS spectra measured at different $p(O_2)$ at A) 600°C, B) 550°C, and C) 500°C.

Figures 5 A–C present the results of the DRT analyses. Three sub-processes can be distinguished, contributing to the impedance response of the electrode – P1, P2, and P3 processes located at a high, medium, and low-frequency range, respectively. The dependence of P1 with decreasing $p(O_2)$ results in a slight increase in the peak area. Moreover, the P1 peak area increases with the decreasing temperature. By comparing the above behaviour with the high-frequency range, it can be attributed to the charge transfer at the electrode/electrolyte interface. The P2 process present in the medium frequency range has a strong dependence on $p(O_2)$ and the temperature. P2 can be associated with various electrode processes described as oxygen surface exchange kinetics and oxygen ion diffusions such as the adsorption of gaseous oxygen O_2, dissociation of O_2, and charge transfer-diffusion (O^{2-}) [30,31]. The last sub-process, P3, occurring at low frequencies, has a strong dependence on $p(O_2)$ only and its peak area increases with the decreasing $p(O_2)$. This process may be related to the gas diffusion process in the porous cathode and it is just slightly dependent on the temperature, but strongly dependent on the microstructural features [32]. The identified electrode processes are identical to the results of other groups performing the DRT analysis of thin LSC electrodes [29,33].

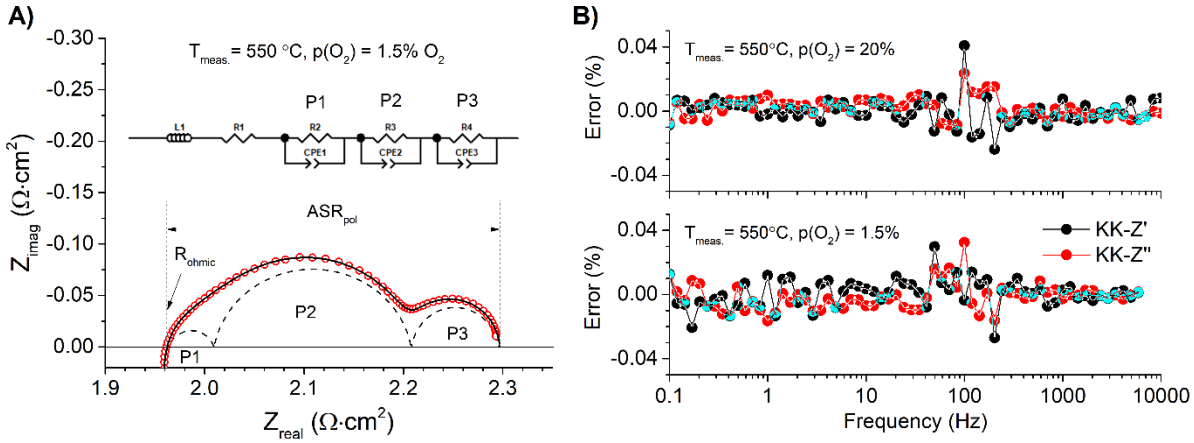

MOST WIEDZY Downloaded from mostwiedzy.pl

Figure 6. A) Detailed deconvolution of EIS for a sample with 400 nm LSC measured at 550°C fitted with an equivalent circuit based on DRT analysis. B) Kramers-Kroning analysis result comparison.

The DRT analysis of the EIS data measured at different $p(O_2)$ and temperatures made it possible to distinguish processes occurring in the investigated electrode and gave a hint for fitting the equivalent circuits to the EIS spectra. Figure 6A presents representative EIS spectra with fitted elements corresponding to the identified electrochemical processes. The equivalent circuit used for fitting consisted of three parallel R||CPE elements (P1, P2, and P3) connected in series with an inductance L and series resistance. Consequently, the model was fitted to all measured impedance spectra, and the collected data allowed us to plot fitting results as the ASR and capacitance characteristics as a function of the oxygen partial pressure summarized in Figure 7. To verify the results of the impedance measurement and establish the validity of the impedance dataset, the Kramers–Kronig test was applied to recorded the spectra [34,35]. Figure 6B presents two plots containing representative test results for the sample exposed for one hour of isothermal holding after temperature reduction and the second one shows the result for the sample exposed for one hour after gas composition change. As can be seen, the K-K transform results overlap, thus demonstrating the selfconsistency of the data. For most of the spectrum, the relative error of both the real and imaginary data was under 0.02%.

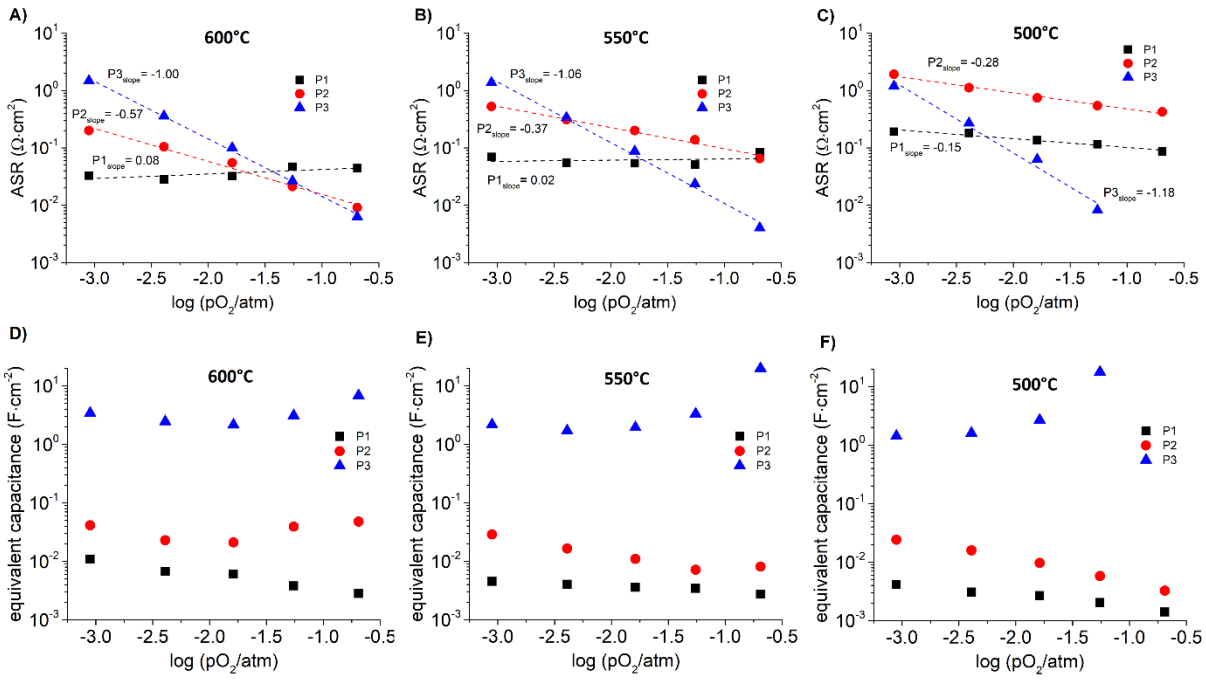

Figure 7. Fitting results of EIS. Plots of calculated resistances and equivalent capacitances of the P1, P2, and P3 contributions as a function of $p(O_2)$ measured at A), D) 600°C, B), E) 550°C and C), F) 500°C.

MOST WIEDZY Downloaded from mostwiedzy.pl

Figure 7 (A-C) presents variations of the ASRs of the identified electrode sub-processes with pO_2. The slope of the curves allows us to determine the possible mechanism of the occurring reaction in the electrodes [36]. For a slope of -0.5 to -0.25, the dependence may be attributed to adsorption and surface exchange, whereas a slope of -1 involves the contribution of molecular oxygen and is attributed to gaseous diffusion. The P3 process is characterised by the greatest variability in the function of pO_2 with a value of slope close to -1 for the investigated temperature range and can be correlated with the gas diffusion reactions in the electrode. The resistances of the two other processes, P1 and P2, are more sensitive to the temperature and have a much smaller slope than P3. For the P2 process, the value of the slope increases with the reducing temperature and varies from -0.58 to -0.28 for 600 and 500°C, respectively. It makes it possible to conclude that this process is related to oxygen surface exchange kinetics and oxygen ion diffusion. In contrast, the process P1 presents an almost flat inclination of a slope but the ASR has thermally activated dependence and increases with the decreasing temperature. Thus, P1 corresponds to the charge transfer reaction at the electrode/electrolyte interface. Looking into details on the resistance values of individual processes in the air atmosphere, it can be seen that at high temperatures, the P1 process related to the charge-transfer reaction at the interface has higher resistance compared to other sub-processes, indicating that P1 is the rate-determining reaction at higher temperatures, but with the decreasing temperature, P2 significantly increases and P2 overtakes P1 at temperatures below 550°C, becoming the rate-determining reaction in the lower temperature range.

To supplement the ASR values, specific pseudocapacitances of the identified sub-processes were calculated and presented in Figure 7 (D-F). For the low-frequency contribution (P3), the equivalent capacitance shows high values and varies between 1.4 to 20 $F \cdot cm^{-2}$ depending on the oxygen concentration and measurement temperature. The low-frequency contribution does not show strong temperature dependence but shows strong oxygen partial pressure dependence. These high capacitance values have a chemical, not electrochemical origin, and are typical for a gas diffusion resistance in porous electrodes. Furthermore, the capacitance of the P2 process is between one to two orders of magnitude lower than for P3, which is typical for the adsorption processes assigned to P2 [37]. The lowest capacitance values were observed for the P1 process ($<10^{-3}$) and can be correlated with the charge transfer process occurring at the interface between the electrode and electrolyte layers.

MOST WIEDZY Downloaded from mostwiedzy.pl

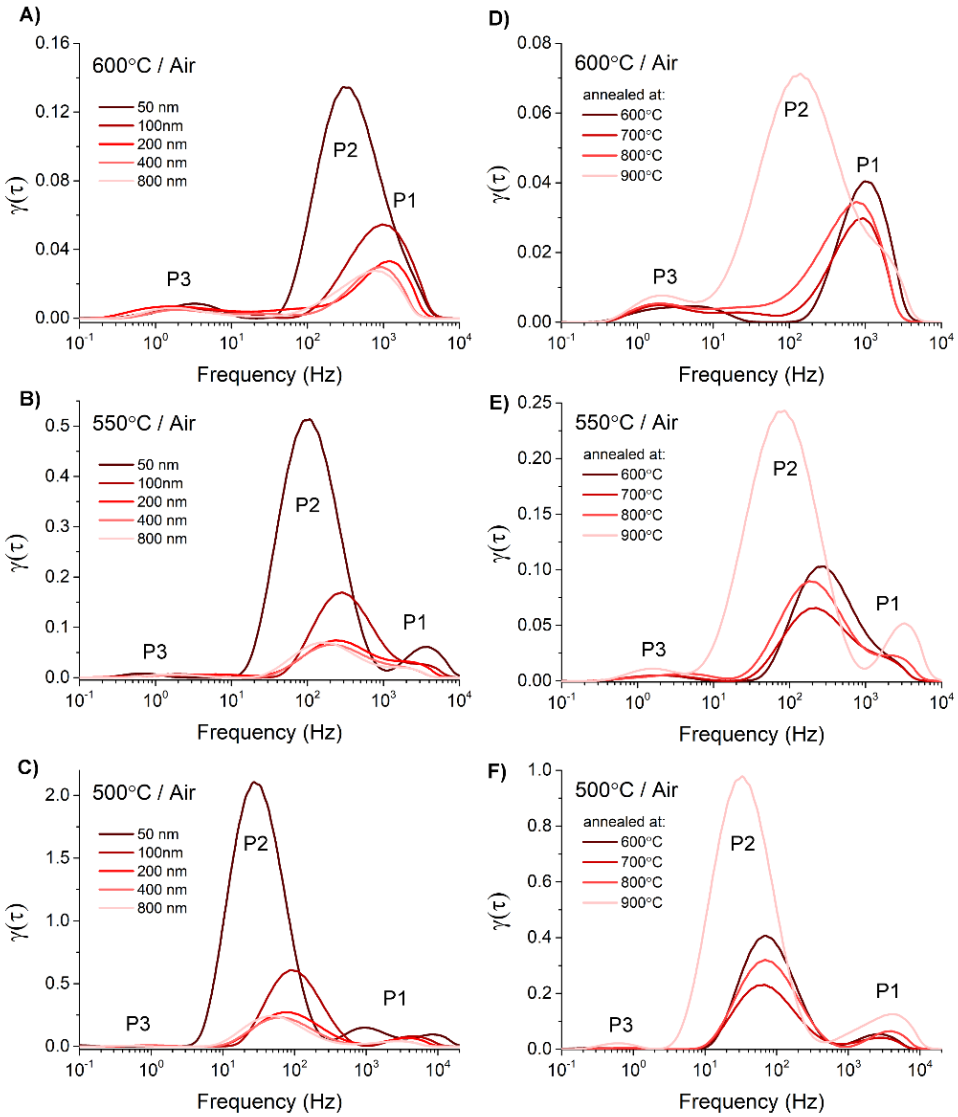

Figure 8. DRT analysis results measured at 600°C, 550°C and 500°C for samples with (A–C) various LSC thicknesseses in a range of 50–800 nm and (D–F) annealed at different temperatures (600–900°C).

The results presented in subsections 3.2.1 and 3.2.2, including the effect of the thickness of the LSC layer and the annealing temperature, were subjected to DRT analysis and the rate-limiting processes taking place in the electrodes was not determined. Figure 8 presents the results of the DRT analysis for the measurements performed in air in the temperature range of 500–600°C. Due to different scales, the result for the reference LSCF sample was presented separately in Figure S2 in supplementary materials. It can be seen that the rate-limiting process for LSFC electrode is related with the P3 process, which has the highest intensity. The introduction of a nanoporous LSC layer (from 50 nm) with a very well developed active surface causes that the gas diffusion process ceases to dominate and becomes a process that does not affect the overall reaction of the electrode. In Figures 8 A–C, the presented results for the sample with a 50 nm LSC layer indicate the dominance of the resistance

MOST WIEDZY Downloaded from mostwiedzy.pl

associated with P2 described as oxygen surface exchange kinetics and oxygen ion diffusion. Nevertheless, increasing the thickness of the LSC layer significantly reduces the peak area by improving the electrode performance. This phenomenon can be attributed to the increase of the triple phase boundary leading to developing the active area surface between three different phases close to the electrode-electrolyte interface. Moreover, the area of the peak correlated with P2 improves and remains almost constant for the layers with thicknesses of 400 nm and 800 nm. This allows the assumption that due to the well-developed microstructure of the LSC layer and the extremely fast kinetics of this MIEC electrode material, the electrochemically active layer thickness near the interface is close to 400 nm. In such a situation, the porous LSCF electrode above the active LSC layer merely acts as a current collector and is not electrochemically active. By analysing the behaviour of the P1 process with increasing layer thickness, a reduction in the process resistance between 50 and 100 nm of the layer thickness can be noticed. A subsequent increase in layer thickness has no significant effect on this process. This fact can be explained by the continuity of the applied layer. The spray pyrolysis technique is a method in which a layer is created by depositing fine droplets from an air-atomised precursor solution on a heated substrate. A continuous layer is formed when the falling droplets of the precursor overlap each other and form a uniform layer. One of the limitations of this method is the need to deposit a certain amount of precursor to obtain a continuous and homogenous layer in terms of thickness. In the case of layers with a thickness of >100 nm, it is possible to obtain homogeneous layers, but below this range, some discontinuities in the coating are visible due to places where the droplets did not spread. This effect was presented in our earlier publication examining the properties of the LSC layer deposited from different amounts of precursor solution [19]. On the other hand, above 1 µm thickness, the droplets overlap and start making clear differences in the thickness of the layer visible in the cross-section images, giving the impression of a wavy surface. The 50 nm thick layer is not a continuous layer and the LSCF is partially in direct contact with the electrolyte. LSC is a material with a higher electronic conductivity than LSCF, therefore the increased resistance of the P1 process for a sample with a 50 nm layer will be related to this phenomenon. The last P3 process related to the gas diffusion reaction in the cathode has the smallest contribution to the electrode resistance. The resistance of this process does not change significantly with the increase of the thickness of the LSC layer and remains almost constant in the analysed temperature range.

Figures 8 D–F show the results of the DRT analysis for a sample with an LSC layer thickness of 400 nm, exposed at different temperatures. The presented graphs show that the dominant process with the highest resistance is the P2 process. Moreover, with the increase of the annealing temperature from 600°C to 700°C, a clear decrease in the P2resistance is observed, and a further increase in the annealing temperature to 800°C causes a slight increase in the resistance, but its value

MOST WIEDZY Downloaded from mostwiedzy.pl

is still lower than for the sample annealed at 600°C. A significant increase in the resistance associated with P2 can only be observed when the sample is exposed to a temperature of 900°C, but slight changes for P1 and P3 are also observed. Referring again to the earlier publication where the influence of the annealing temperature on the microstructural and electrical properties of the layer was investigated, it can be concluded that it is the change in the microstructure and electrical conductivity of the LSC layer that is directly responsible for the increase in the resistance of the sample exposed to 900°C [19].

3.2.4 Durability of the electrodes

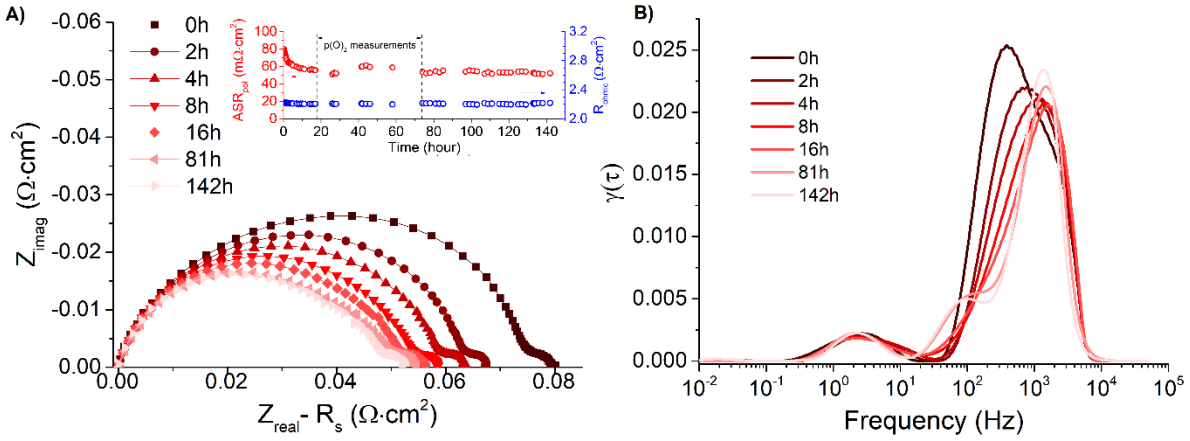

Figure 9. Long-term stability test A) Nyquist plot B) DRT analysis result.

Grain growth and densification of the nanocrystalline and nanoporous material is one of the potential problems due to the high operating temperatures, which consequently leads to a reduction of the active surface area. The long-term stability test was maintained as a continuation of the measurement of the samples tested at different $p(O_2)$ and lasted over 140 h in total. The sample was held in isothermal conditions at 600°C in the air atmosphere except for the testing times in different oxygen partial pressures. Figure 9A presents a Nyquist plot with EIS spectra collected at various times during the test. The inset in the diagram also shows the change in R_{ohmic} and R_{pol} values throughout the experiment. As can be seen, the ohmic resistance (R_{ohmic}) remains constant throughout the experiment. This proves the good adhesion of the layer to the electrolyte and the absence of any adverse reaction between the layer and the electrolyte. On the other hand, the graph of the polarisation resistance (R_{pol}) change over time shows a decrease in the resistance value after the first 10 h and its stabilisation at around 55 mΩ·cm^2. This is a significant improvement in the performance of the electrode. As shown above, in section 3.2.2, the increase of the annealing temperature from 600°C to 700°C results in a decrease in the polarisation resistance, and thus the extended annealing time of the sample previously sintered at 600°C also has a positive effect on the microstructure relaxation by reducing the value of

MOST WIEDZY Downloaded from mostwiedzy.pl

the polarisation resistance. By analysing the results of the EIS spectra utilising the DRT method, it is visible that a change took place at a medium frequency related to electrochemical reactions at the surface of the electrode, described above as a P2 sub-process. This phenomenon may be also related to the improvement of the electrical conductivity of LSC observed in previous studies [20]. The electrical conductivity of the LSC layer deposited on the sapphire increased by 20% in the first 10 hours of the isothermal holding. Such a significant improvement affects the efficiency of reactions related to oxygen surface exchange kinetics and oxygen ion diffusions such as the adsorption of gaseous oxygen O_2, dissociation of O_2, and charge transfer-diffusion (O^{2-}).

3.2.5 SOFC ageing test

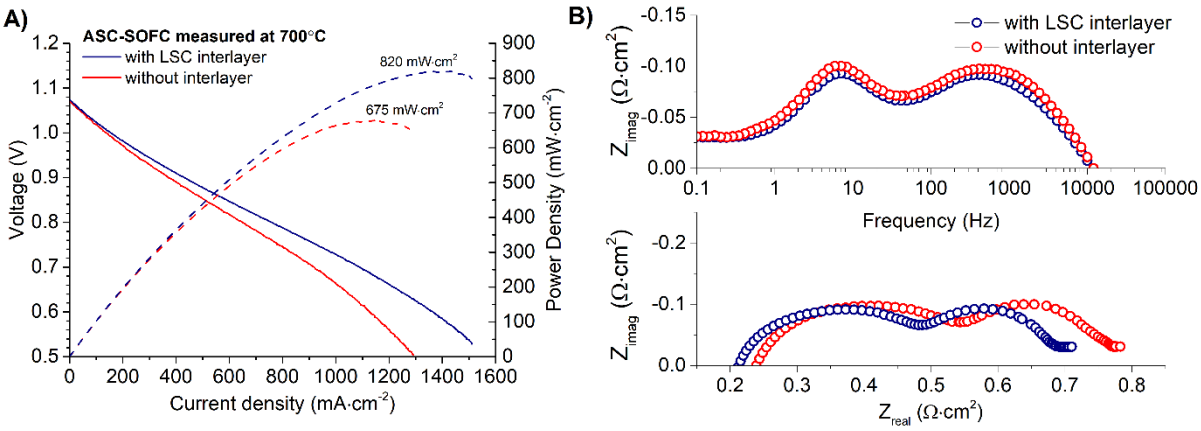

Figure 10. Initial performance of prepared ASC-SOFCs with reference and developed electrodes. A) Current-Voltage characteristics and B) Bode and Nyquist plots measured in OCV at 700°C.

A fuel cell test was performed to determine the electrochemical performance of the developed electrode. For this purpose, two anode-supported cells were compared, a reference cell and a cell with an LSC interlayer at the interface. Figure 10 presents the current-voltage characteristics and impedance measurement results measured at the beginning of the measurement was taken after reduction process. The two cells show the same OCV values of 1.07 V. The maximum power density reaches 675 and 820 mW·cm^{-2} for the reference cell and the cell with the LSC interlayer, respectively. The initial ohmic and polarisation resistances for the modified electrode were 0.21 Ω·cm^2 and 0.5 Ω·cm^2, whereas, for the unmodified sample, they were 0.24 Ω·cm^2 and 0.55 Ω·cm^2. As can be seen, there is a clear improvement in the efficiency of the cell with the modified electrode (by approx. 20%). Sung Soo Shin et al. also investigated the nanoscale interlayer of cathodes in low-temperature solid oxide fuel cells and achieved a similar improvement in reference to cells without an interlayer. The higher power densities achieved by this group may result from the use of a thinner YSZ electrolyte and more precise methods of applying the buffer layer (PLD) and active layer (precursor-solution electrospray method) [38]. Another piece of research presented by Solovyev et al. also reveals a significant improvement of an

MOST WIEDZY Downloaded from mostwiedzy.pl

anode-supported cell by 1.6 times at 700°C by utilising a sputter-deposited 600 nm thick LSC interlayer between the LSC electrode and the CGO electrolyte [39]. Moreover, the obtained results are comparable with the previous performance of the cells on the same type of anode substrates, where the CGO barrier layer was investigated, but in this case, the operating temperature of the cell was lowered by 50°C [21]. Therefore, it was possible to maintain the efficiency of the cells by lowering the operating temperature, which was the aim of this study.

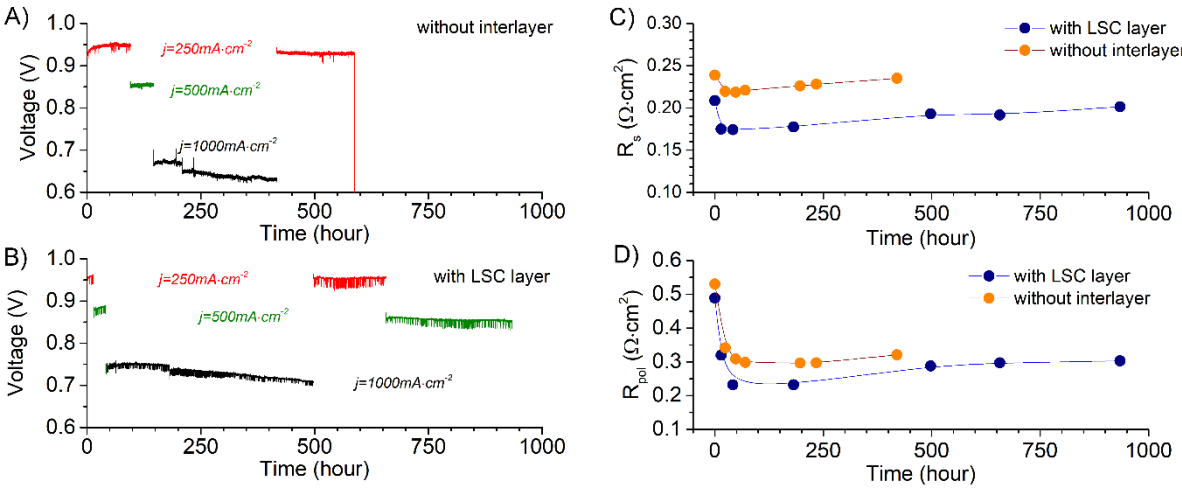

Figure 11. Long-term stability test under load. A) and B) Voltage as a function of time plots for reference and modified electrode cells working under load. C) Ohmic resistance and D) polarisation resistance change as a function of time.

Figures 11 A and B show graphs of voltage as a function of time with a different cell loads. The voltage under a load of 250 mA·cm^2 is marked in red, 500 mA·cm^2 is marked in green, and 1 A·cm^2 is black. Long-term stability tests were carried out for almost 950h for the modified cell, and 600h for the reference cell. The shorter duration of the reference experiment resulted from an unexpected power failure. The target test was to check the cell degradation under a high load of 1 A·cm^2, therefore at the beginning of the experiment, both cells were loaded with a current of 250 and 500 A·cm^2 for initial stabilisation, and then the current was increased to the target values of 1 A·cm^2. The degradation rate values at high current densities were 0.17 mV/h for the reference cell and 0.1 mV/h for the cell with LSC at the interface. It showed better resistance to degradation and better performance of the cell with an LSC layer on the interface. In addition, impedance measurements at OCV were carried out from time to time to record changes in the resistance of the cells during the experiment. The measured values of the ohmic and polarisation resistances are presented in the form of graphs in Figures 11 C and D, respectively. The nature of the curves plotted on the measurement points indicates similar changes in the resistance value with the difference being that the values for the cell with the LSC interlayer are lower. The lowest values of ohmic and polarisation resistances were recorded after

MOST WIEDZY Downloaded from mostwiedzy.pl

about 50 hours of cell operation under load and were R_{pol} = 0.298, 0.231 Ω·cm^2, and R_s = 0.218, 0.174 Ω·cm^2 for the reference and modified sample, respectively. The same character of changes in the resistance values over time, regardless of whether a reference or a modified cathode was used, suggests changes occurring in the anode part of the cell and can be explained by the evolution of the morphology of the anode bulk previously observed by Zhang et al.[40]

Additional Figure S3 in supplementary materials presents a modified electrode-electrolyte interface cross-section of the fuel cell after the ageing test at 700°C for almost 1000h. As can be noticed, the interlayer microstructure changed over a long operation time under load. The interlayer microstructure after the test changed significantly from those presented in Figure S1B - reference after annealing at 700°C for 2 hours. Nanoparticles became coarser, but the electrochemical efficiency remained stable and still presented better results than the reference sample without interlayer.

4. Conclusions

In this work, an $La_{0.6}Sr_{0.4}CoO_{3-d}$ oxygen electrode material was deposited between a dense $Ce_{0.8}Gd_{0.2}O_{2-d}$ electrolyte and a porous $La_{0.6}Sr_{0.4}Co_{0.2}Fe_{0.8}O_{3-d}$ electrode by the spray pyrolysis technique. The developed oxygen electrode interface was investigated utilising electrochemical impedance spectroscopy and distribution of relaxation times analysis. The material tests were carried out for various LSC layer thicknesses, annealing temperatures, oxygen partial pressures, and temperatures, and were subjected to long-term stability tests and evaluated in typical operating conditions in an intermediate temperature SOFC.

Structural studies confirmed the presence of a single-phase nanocrystalline LSC crystallised in a cubic perovskite structure. In addition, phase analysis of the interface cross-section did not indicate interfacial reactions between the electrode and electrolyte or segregation inside the layer. Electrochemical investigations proved that the addition of even a very thin layer (approx. 50 nm) of LSC at the interface measurably reduces the polarisation resistance, which is further improved by increasing the thickness of the interfacial layer. The lowest polarisation resistance values were obtained for a layer with a thickness of 400 nm, annealed at a temperature of 700°C and the ASR_{pol} values measured at 600°C were 0.349; 0.145; 0.105; 0.079, and 0.076 Ω·cm^2 for samples with 50, 100, 200, 400 and 800 nm of LSC interlayer thickness, while ASR_{pol} for a reference LSCF without interface modification was 0.77Ω·cm^2. Studies over a wide range of oxygen partial pressures and temperatures identified three electrochemical processes in the modified electrode. The identified reactions were: P1 – charge transfer reaction at the electrode/electrolyte interface; P2 – oxygen surface exchange kinetics and oxygen ion diffusion; P3 – gas diffusion reaction in the cathode. It was found that the process limiting further efficiency improvement is related to P2, while in the long-term tests, the resistance of

MOST WIEDZY Downloaded from mostwiedzy.pl

P2 decreased, making the P1 process dominant after some time. After the initial stabilisation in the ageing tests, the electrode did not degrade during the following hours, and both R_{pol} and R_{ohmic} remained stable over time.

Finally, the electrode was tested in a working fuel cell. The tests showed increased electrode performance by 20% compared to an unmodified electrode. The maximum power density reached 675 and 820 $mW \cdot cm^{-2}$ for the reference cell and the cell with the LSC interlayer, respectively. Ageing tests under high load showed an almost twofold lower degradation rate.

In summary, it was possible to produce an electrode with a highly developed active surface at the electrode-electrolyte interface, which decreased the resistance values and contributed to an increase in electrochemical efficiency in the cell. The nanocrystalline and nanoporous LSC layer produced by spray pyrolysis was responsible for increasing the cell's performance. The main goal of the work, lowering the operating temperature of the cell while maintaining high electrochemical efficiency, was achieved.

5. Acknowledgements

The presented research is part of the "Nanocrystalline ceramic materials for efficient electrochemical energy conversion" project, carried out within the First TEAM program of the Foundation for Polish Science (grant agreement no. POIR.04.04.00-00-42E9/17-00), co-financed by the European Union under the European Regional Development Fund. The statutory fund of WETI PG is also acknowledged.

6. Supporting Information

Cross-section SEM images of electrode-electrolyte interface microstructure annealed at different temperatures. DRT analysis results for reference LSCF electrode. SEM freacture image of electrode-electrolyte interface of anode supported fuel cell after 1000h test under load.

7. Bibliography

(1) Zhu, B.; Fan, L.; Mushtaq, N.; Raza, R.; Sajid, M.; Wu, Y.; Lin, W.; Kim, J. S.; Lund, P. D.; Yun, S. Semiconductor Electrochemistry for Clean Energy Conversion and Storage; *Electrochem. Energy Rev.* **2021**, 4, 757–792. https://doi.org/10.1007/s41918-021-00112-8.

(2) IEA (2021), Global Hydrogen Review 2021, *OECD Publishing*, **2021**. https://doi.org/10.1787/39351842-en.

(3) Stambouli, A. B.; Traversa, E. Solid Oxide Fuel Cells (SOFCs): A Review of an Environmentally

MOST WIEDZY Downloaded from mostwiedzy.pl

Clean and Efficient Source of Energy. *Renew. Sustain. Energy Rev.* **2002**, *6* (5), 433–455. https://doi.org/10.1016/S1364-0321(02)00014-X.

(4) Minh, N. Q. Ceramic Fuel Cells. *J. Am. Ceram. Soc.* **1993**, *76* (3), 563–588. https://doi.org/10.1111/j.1151-2916.1993.tb03645.x.

(5) Zhang, Y.; Knibbe, R.; Sunarso, J.; Zhong, Y.; Zhou, W.; Shao, Z.; Zhu, Z. Recent Progress on Advanced Materials for Solid-Oxide Fuel Cells Operating Below 500 °C. *Adv. Mater.* **2017**, *29* (48), 1700132. https://doi.org/10.1002/adma.201700132.

(6) Wachsman, E. D.; Lee, K. T. Lowering the Temperature of Solid Oxide Fuel Cells. *Science.* **2011**, *334* (6058), 935–939. https://doi.org/10.1126/science.1204090.

(7) Oh, E. O.; Whang, C. M.; Lee, Y. R.; Park, S. Y.; Prasad, D. H.; Yoon, K. J.; Son, J. W.; Lee, J. H.; Lee, H. W. Extremely Thin Bilayer Electrolyte for Solid Oxide Fuel Cells (SOFCs) Fabricated by Chemical Solution Deposition (CSD). *Adv. Mater.* **2012**, *24* (25), 3373–3377. https://doi.org/10.1002/adma.201200505.

(8) Chen, G.; Sun, W.; Luo, Y.; He, Y.; Zhang, X.; Zhu, B.; Li, W.; Liu, X.; Ding, Y.; Li, Y.; Geng, S.; Yu, K. Advanced Fuel Cell Based on New Nanocrystalline Structure $Gd_{0.1}Ce_{0.9}O_2$ Electrolyte. *ACS Appl. Mater. Interfaces* **2019**, *11* (11), 10642–10650. https://doi.org/10.1021/acsami.8b20454.

(9) Adler, S. B. Factors Governing Oxygen Reduction in Solid Oxide Fuel Cell Cathodes. *Chem. Rev.* **2004**, *104* (10), 4791–4843. https://doi.org/10.1021/cr020724o.

(10) Zhang, Y.; Nicholas, J. D.; Soc, J. E.; Zhang, Y. Updating the Notion That Poor Cathode Performance Typically Dominates Overall Solid Oxide Fuel Cell Response Updating the Notion That Poor Cathode Performance Typically Dominates Overall Solid Oxide Fuel Cell Response. *J. Electrochem. Soc.* **2021,** 168, 034513. https://doi.org/10.1149/1945-7111/abed21.

(11) Barfod, R.; Hagen, A.; Ramousse, S.; Hendriksen, P. V; Mogensen, M. Break Down of Losses in Thin Electrolyte SOFCs. *Fuel Cells* **2006**, 6 (2), 141–145. https://doi.org/10.1002/fuce.200500113.

(12) Vohs, J. M.; Gorte, R. J. High-Performance SOFC Cathodes Prepared by Infiltration. *Adv. Mater.* **2009**, *21* (9), 943–956. https://doi.org/10.1002/adma.200802428.

(13) Zapata-Ramírez, V.; Dos Santos-Gómez, L.; Mather, G. C.; Marrero-López, D.; Pérez-Coll, D. Enhanced Intermediate-Temperature Electrochemical Performance of Air Electrodes for Solid Oxide Cells with Spray-Pyrolyzed Active Layers. *ACS Appl. Mater. Interfaces* **2020**, *12* (9),

MOST WIEDZY Downloaded from mostwiedzy.pl

10571–10578. https://doi.org/10.1021/acsami.9b22966.

(14) Fan, L.; Zhu, B.; Su, P. C.; He, C. Nanomaterials and Technologies for Low Temperature Solid Oxide Fuel Cells: Recent Advances, Challenges and Opportunities. *Nano Energy* **2018**, *45*, 148–176. https://doi.org/10.1016/j.nanoen.2017.12.044.

(15) dos Santos-Gómez, L.; Zamudio-García, J.; Porras-Vázquez, J. M.; Losilla, E. R.; Marrero-López, D. Recent Progress in Nanostructured Electrodes for Solid Oxide Fuel Cells Deposited by Spray Pyrolysis. *J. Power Sources* **2021**, *507*, 230277. https://doi.org/10.1016/j.jpowsour.2021.230277.

(16) Chen, X.; Grande, T. Anisotropic Chemical Expansion of $La_{1-x}Sr_xCoO_{3-\delta}$. *Chem. Mater.* **2013**, *25* (6), 927–934. https://doi.org/10.1021/cm304040p.

(17) Brett, D. J. L.; Atkinson, A.; Brandon, N. P.; Skinner, S. J. Intermediate Temperature Solid Oxide Fuel Cells. *Chem. Soc. Rev.* **2008**, *37* (8), 1568–1578. https://doi.org/10.1039/b612060c.

(18) Kim, J. H.; Jang, K. L.; Ahn, K.; Yoon, T.; Lee, T. I.; Kim, T. S. Thermal Expansion Behavior of Thin Films Expanding Freely on Water Surface. *Sci. Rep.* **2019**, *9* (1), 1–7. https://doi.org/10.1038/s41598-019-43592-x.

(19) Kamecki, B.; Karczewski, J.; Abdoli, H.; Chen, M.; Jasiński, G.; Jasiński, P.; Molin, S. Deposition and Electrical and Structural Properties of $La_{0.6}Sr_{0.4}CoO_3$ Thin Films for Application in High-Temperature Electrochemical Cells. *J. Electron. Mater.* **2019**, *48* (9), 5428–5441. https://doi.org/10.1007/s11664-019-07372-7.

(20) Kamecki, B.; Karczewski, J.; Jasiński, P.; Molin, S. Improvement of Oxygen Electrode Performance of Intermediate Temperature Solid Oxide Cells by Spray Pyrolysis Deposited Active Layers. *Adv. Mater. Interfaces* **2021**, *8*, 2002227. https://doi.org/10.1002/admi.202002227.

(21) Molin, S.; Karczewski, J.; Kamecki, B.; Mroziński, A.; Wang, S.; Jasiński, P. Processing of $Ce_{0.8}Gd_{0.2}O_{2-\delta}$ Barrier Layers for Solid Oxide Cells : The Effect of Preparation Method and Thickness on the Interdiffusion and Electrochemical Performance. *J. Eur. Ceram. Soc.* **2020**, *40*, 5626–5633. https://doi.org/10.1016/j.jeurceramsoc.2020.06.006.

(22) Hołówko, B.; Karczewski, J.; Molin, S.; Jasiński, P. Preparation of Hydrogen Electrodes of Solid Oxide Cells by Infiltration : E Ff Ects of the Preparation Procedure on the Resulting Microstructure. *Materials (Basel).* **2020**, *13* (131).

(23) Koch S, Graves C, H. K. *Elchemea Analytical (Open source free software)*.

MOST WIEDZY Downloaded from mostwiedzy.pl

https://www.elchemea.dk/.

(24) T.H. Wan, M. Saccoccio, C. Chen, F. C. Influence of the Discretization Methods on the Distribution of Relaxation Times Deconvolution: Implementing Radial Basis Functions with DRTtools. *Electrochim. Acta* **2015**, *184*, 483–499.

(25) Kubicek, M.; Rupp, G. M.; Huber, S.; Penn, A.; Opitz, A. K.; Bernardi, J.; Stöger-Pollach, M.; Hutter, H.; Fleig, J. Cation Diffusion in $La_{0.6}Sr_{0.4}CoO_{3-\delta}$ below 800°C and Its Relevance for Sr Segregation. *Phys. Chem. Chem. Phys.* **2014**, *16* (6), 2715–2726. https://doi.org/10.1039/c3cp51906f.

(26) Liu, M. Equivalent Circuit Approximation to Porous Mixed-Conducting Oxygen Electrodes in Solid-State Cells. *J. Electrochem. Soc.* **1998**, *145* (1), 142–154. https://doi.org/10.1149/1.1838227.

(27) Cohn, G.; Wachsman, E. D. In-Operando Determination of SOFC Cathode Oxygen Surface Exchange Coefficients for Enhanced Oxygen Reduction Reaction Kinetics. *J. Electrochem. Soc.* **2017**, *164* (10), F3035–F3044. https://doi.org/10.1149/2.0411708jes.

(28) Hayd, J.; Dieterle, L.; Guntow, U.; Gerthsen, D.; Ivers-Tiffée, E. Nanoscaled La0.6Sr0.4CoO3-δ as Intermediate Temperature Solid Oxide Fuel Cell Cathode: Microstructure and Electrochemical Performance. *J. Power Sources* **2011**, *196* (17), 7263–7270. https://doi.org/10.1016/j.jpowsour.2010.11.147.

(29) Develos-Bagarinao, K.; Celikbilek, O.; Budiman, R. A.; Kerherve, G.; Fearn, S.; Skinner, S. J.; Kishimoto, H. On the Role of Surfaces and Interfaces in Electrochemical Performance and Long-Term Stability of Nanostructured LSC Thin Film Electrodes. *J. Mater. Chem. A* **2022**, *10* (5), 2445–2459. https://doi.org/10.1039/d1ta07235h.

(30) Adler, S. B. Limitations of Charge-Transfer Models for Mixed-Conducting Oxygen Electrodes. *Solid State Ionics* **2000**, *135* (1–4), 603–612. https://doi.org/10.1016/S0167-2738(00)00423-9.

(31) Fu, C.; Sun, K.; Zhang, N.; Chen, X.; Zhou, D. Electrochemical Characteristics of LSCF-SDC Composite Cathode for Intermediate Temperature SOFC. *Electrochim. Acta* **2007**, *52* (13), 4589–4594. https://doi.org/10.1016/j.electacta.2007.01.001.

(32) Jacobsen, T.; Hendriksen, P. V.; Koch, S. Diffusion and Conversion Impedance in Solid Oxide Fuel Cells. *Electrochim. Acta* **2008**, *53* (25), 7500–7508. https://doi.org/10.1016/j.electacta.2008.02.019.

(33) Develos-Bagarinao, K.; Budiman, R. A.; Ishiyama, T.; Yamaji, K.; Kishimoto, H. Leveraging

MOST WIEDZY Downloaded from mostwiedzy.pl

Catalytic Effects of Heterointerfaces through Multilayering for Superior Cathode Performance. *J. Power Sources* **2020**, *480*, 229094. https://doi.org/10.1016/j.jpowsour.2020.229094.

(34) Boukamp, B. A. A Linear Kronig-Kramers Transform Test for Immittance Data Validation. *J. Electrochem. Soc.* **1995**, *142* (6), 1885–1894. https://doi.org/10.1149/1.2044210.

(35) Schönleber, M.; Klotz, D.; Ivers-Tiffée, E. A Method for Improving the Robustness of Linear Kramers-Kronig Validity Tests. *Electrochim. Acta* **2014**, *131*, 20–27. https://doi.org/10.1016/j.electacta.2014.01.034.

(36) Esquirol, A.; Brandon, N. P.; Kilner, J. A.; Mogensen, M. Electrochemical Characterization of $La_{0.6}Sr_{0.4}Co_{0.2}Fe_{0.8}O_3$ Cathodes for Intermediate-Temperature SOFCs. *J. Electrochem. Soc.* **2004**, *151* (11), A1847. https://doi.org/10.1149/1.1799391.

(37) Mroziński, A.; Molin, S.; Karczewski, J.; Miruszewski, T.; Jasiński, P. Electrochemical Properties of Porous $Sr_{0.86}Ti_{0.65}Fe_{0.35}O_3$ Oxygen Electrodes in Solid Oxide Cells: Impedance Study of Symmetrical Electrodes. *Int. J. Hydrogen Energy* **2019**, *44* (3), 1827–1838. https://doi.org/10.1016/j.ijhydene.2018.11.203.

(38) Shin, S. S.; Kim, J. H.; Li, G.; Lee, S. Y.; Son, J. W.; Kim, H.; Choi, M. A Highly Activated and Integrated Nanoscale Interlayer of Cathodes in Low-Temperature Solid Oxide Fuel Cells via Precursor-Solution Electrospray Method. *Int. J. Hydrogen Energy* **2019**, *44* (9), 4476–4483. https://doi.org/10.1016/j.ijhydene.2018.11.143.

(39) Solovyev, A. A.; Shipilova, A. V.; Ionov, I. V.; Smolyanskiy, E. A.; Nikonov, A. V.; Pavzderin, N. B. The Performance of Intermediate Temperature Solid Oxide Fuel Cells with Sputter Deposited La1-XSrxCoO3 Interlayer. *J. Electroceramics* **2020**, *45* (4), 156–163. https://doi.org/10.1007/s10832-021-00235-w.

(40) Zhang, T.; Zhao, Y.; Zhang, X.; Zhang, H.; Yu, N.; Liu, T.; Wang, Y. Thermal Stability of an in Situ Exsolved Metallic Nanoparticle Structured Perovskite Type Hydrogen Electrode for Solid Oxide Cells. *ACS Sustain. Chem. Eng.* **2019**, *7* (21), 17834–17844. https://doi.org/10.1021/acssuschemeng.9b04350.

MOST WIEDZY Downloaded from mostwiedzy.pl

FOR TABLE AND CONTENTS ONLY:

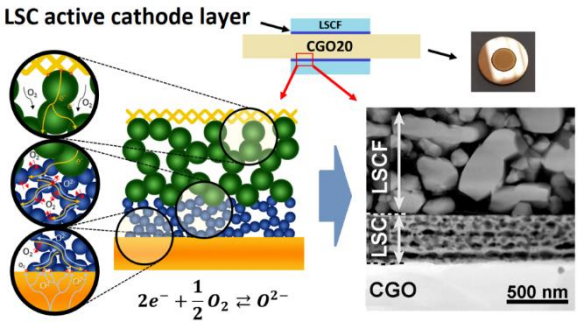

MOST WIEDZY Downloaded from mostwiedzy.pl

Supporting Information

Tuning electrochemical performance by microstructural optimisation of nanocrystalline functional oxygen electrode layer for Solid Oxide Cells

Bartosz Kamecki[1,2*], Grzegorz Cempura[3], Piotr Jasiński[2], Sea-Fue Wang[4], Sebastian Molin[2]

[1] Advanced Materials Center, Faculty of Applied Physics and Mathematics, Gdańsk University of Technology, Gabriela Narutowicza street 11/12, 80-233 Gdańsk, Poland

[2] Advanced Materials Center, Faculty of Electronics, Telecommunications, and Informatics, Gdańsk University of Technology, Gabriela Narutowicza street 11/12, 80-233 Gdańsk, Poland

[3] International Centre for Electron Microscopy, Faculty of Metals Engineering and Industrial Computer Science, AGH University of Science and Technology, Adama Mickiewicza street 30, 30-059 Kraków, Poland

[4] Department of Materials and Mineral Resources Engineering, National Taipei University of Technology, No.1, Sec. 3, Zhongxiao E. Rd., Taipei, 106, Taiwan

*corresponding author: bartosz.kamecki@pg.edu.pl

MOST WIEDZY Downloaded from mostwiedzy.pl

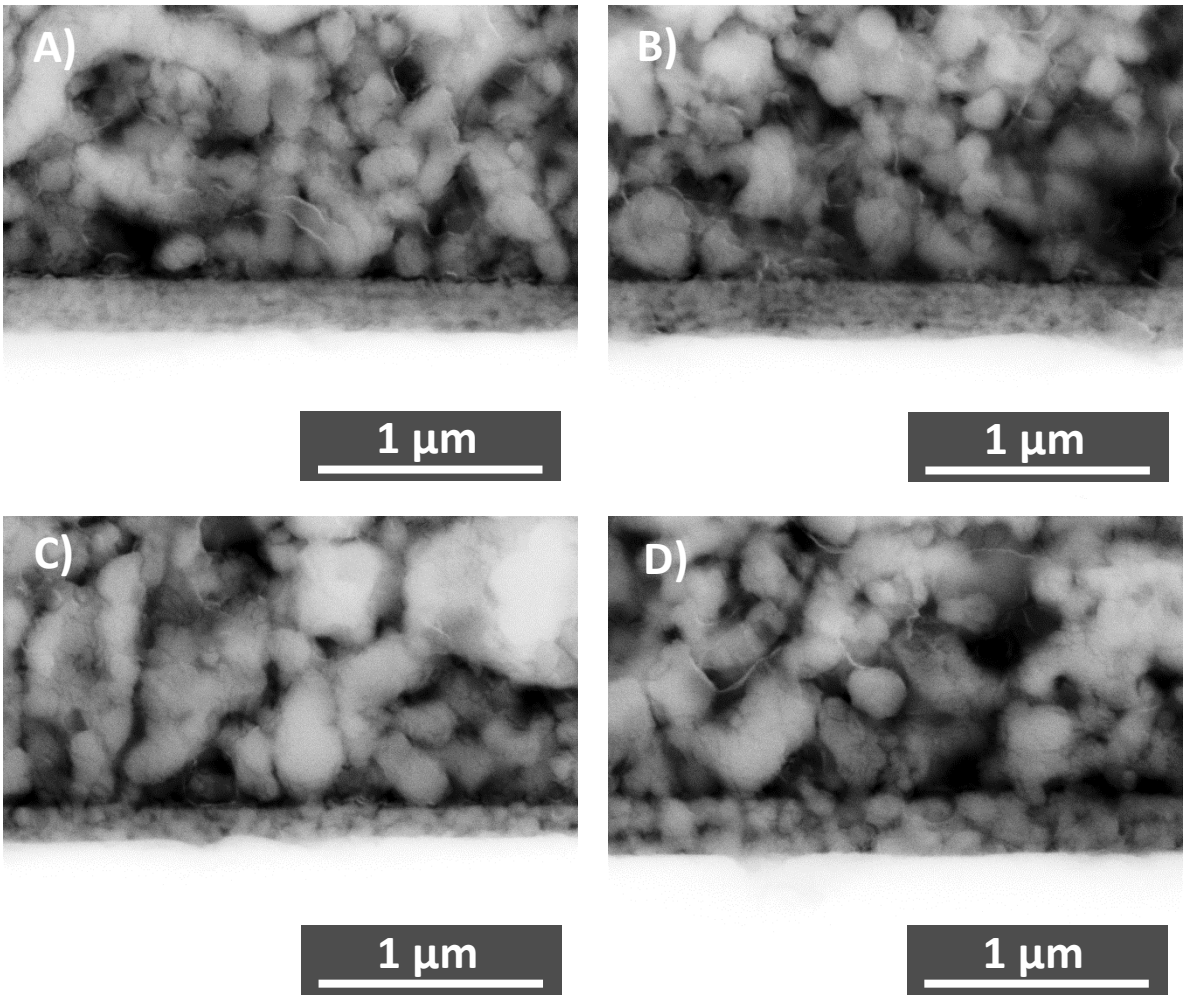

Figure S1. Cross-section SEM images of electrode-electrolyte interface microstructure annealed at A) 600°C, B) 700°C, C) 800°C, D) 900°C for 2h.

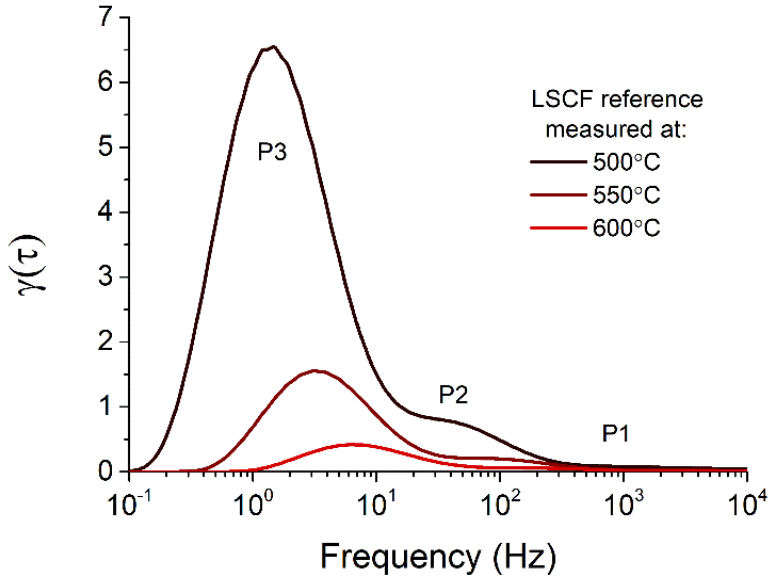

Figure S2. DRT analysis results measured at 600°C, 550°C and 500°C for reference LSCF electrode annealed at 1050°C for 2h.

MOST WIEDZY Downloaded from mostwiedzy.pl

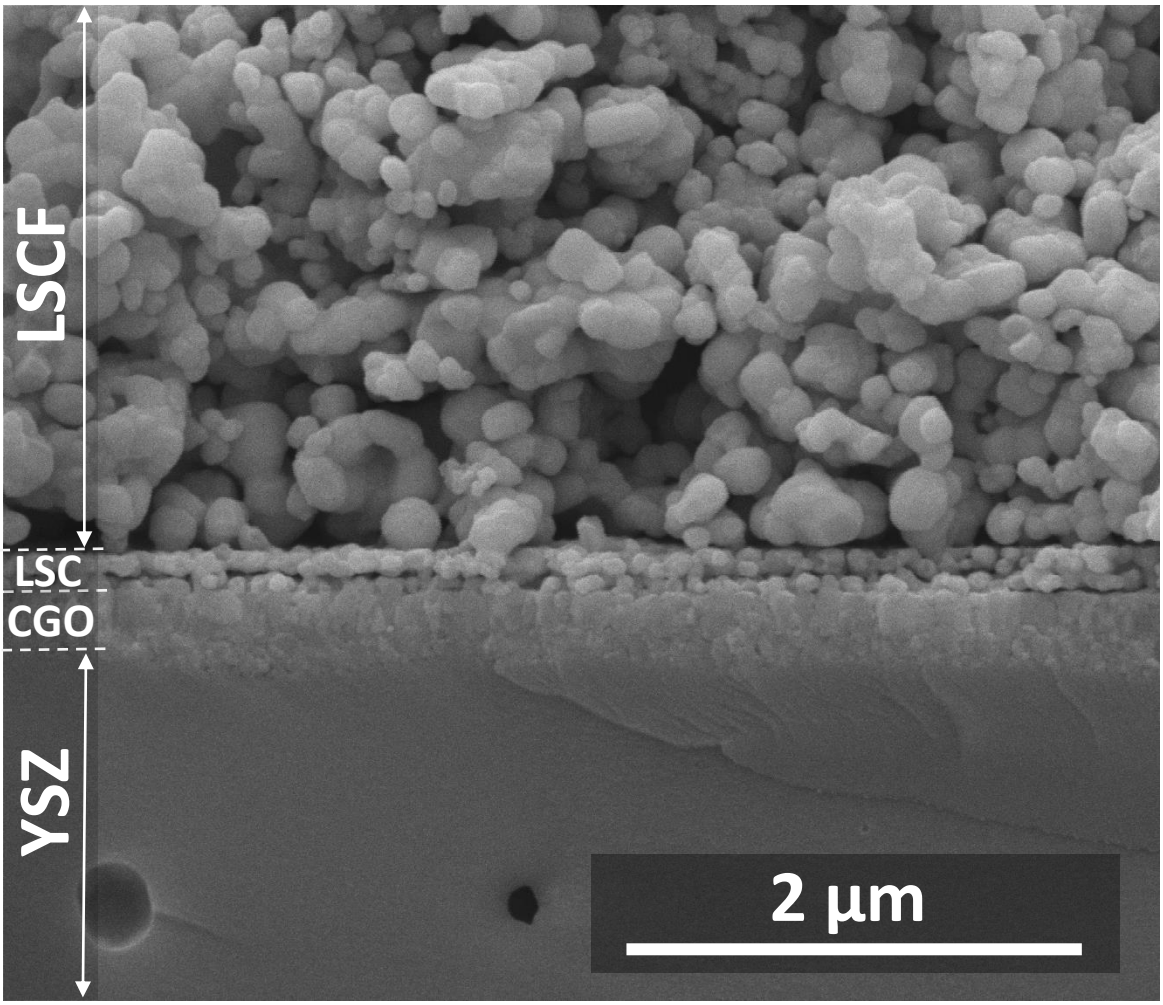

Figure S3. SEM freacture image of electrode-electrolyte interface of anode supported fuel cell with LSC interlayer after 1000h aging at 700°C under high load.

MOST WIEDZY Downloaded from mostwiedzy.pl